Single-Photon Detectors in the Terahertz Range

Susumu Komiyama

(Invited Paper)

***Abstract*—Semiconductor quantum dot detectors as well as semiconductor charge-sensitive infrared phototransistors are described. They are the only detectors that can count single photons in the terahertz region at present. In terms of the noise equivalent power (NEP), the detectors realize experimental values on the order of 10^{-21} W/Hz$^{1/2}$, while theoretically expected values are even much lower, on the order of 10^{-24} W/Hz$^{1/2}$. These NEP values are by several orders of magnitude lower than any other state-of-the-art highly sensitive detectors. In addition to the outstanding sensitivity, the detectors are featured by strong advantage of huge current responsivity (10^6–10^{10} A/W) and extremely large dynamic range of response (10^6–10^8). The mechanism of detection as well as application of the detectors is discussed.**

***Index Terms*—Photon-counting detector, quantum dot (QD), quantum well (QW), single-electron transistor (SET), terahertz (THz).**

I. Introduction

SINGLE-PHOTON-COUNTING method has been established in the spectral regions of X-ray, UV, visible, and near infrared for detecting extremely weak radiation. The technique provides researchers with indispensable tools for the studies of material science, biology, and astrophysics. In the wavelength range up to $\lambda \sim 1.5$ μm, one has a variety of photon detectors including photomultiplier tubes and semiconductor avalanche diodes [1]. Superconducting hot electron bolometers (transition edge sensors) are available up to $\lambda \sim 2.5$ μm [2], [3].

In the long-wavelength range ($\lambda > 10$ μm, frequencies lower than 30 THz), called terahertz (THz) region, however, photon energies are far smaller ($h\nu < 124$ meV for $\lambda > 10$ μm) and the single-photon detection is no longer trivial. Nevertheless, the THz region is one of the richest areas of spectroscopy of matters, encompassing the rotational spectra of molecules, vibrational spectra of molecules, liquids and solids, and the electron energy spectra in semiconductor nanostructures and superconducting energy gap in metals. Hence, sensitive microscopy of matters with high spatial resolution in this spectral region would provide a unique powerful tool for investigation of matters. Unprecedentedly, sensitive observation is also strongly demanded in astrophysics [4]. In the last decade, a variety of novel detection schemes have been proposed [5]–[11]. Among them, only semiconductor quantum devices have demonstrated single-photon detection [6]–[9]: The experimentally achieved noise equivalent power (NEP), less than 1×10^{-20} W/Hz$^{1/2}$, is by several orders of magnitude lower than those of any other detectors. A series of these THz-photon detectors have been implemented in semiconductor nanostructures by introducing ingenious schemes for respective wavelengths from 14 μm up to 0.5 mm [6]–[9]. One of these detectors has been successfully applied for photon-counting THz imaging of low-temperature electron systems [12]–[14]. Another detector has been incorporated in microscopes to realize near-field passive microscopy with subwavelength resolution [15], [16]. In addition, an on-tip device of generating, propagating and detecting single-THz photons has been explored [17]. New metrologies in terms of single-THz photons are thus beginning to emerge.

The purpose of this paper is to describe semiconductor THz single-photon detectors. They are divided into two groups. In one group, called quantum dot (QD) detectors, a QD is electrically polarized by photoexcitation and the induced polarization is sensed by a nearby single-electron transistor (SET) [6]–[8]. In the other group, called charge-sensitive IR phototransistors (CSIPs), an isolated quantum well (QW) island is charged up by photoexcitation, and the induced charge is detected by a conducting channel of 2-D electron gas (2DEG) [9], [18]. The detection scheme is similar between the two groups of detectors; namely, 1) excitation energy is stored in a nanoscale capacitor in the form of a charging energy $\varepsilon_{\rm ch} \approx 0.3$ $\sim$1 meV $\gg k_B T$ (T, the detector temperature) and 2) the charged-up state is sufficiently long lived (10 μs to 1s) to be detected by a conductance change of a nearby charge-sensitive detector. The charge-up state is not disturbed by thermal fluctuation because $\varepsilon_{\rm ch} \gg k_B T$, and the induced current pulse is of sufficiently long duration to be detected beyond the Johnson or the shot noise.

In this paper, fundamental mechanism of the semiconductor THz single-photon counters is reviewed by highlighting the fundamental concept underlying these devices. Theoretical analysis of sensitivity is also provided to discuss future potential development of these detectors.

II. General Scheme

Photo-induced current in a photoconductive detector is generally written as follows:

$$I_{\rm sig} = G_{\rm PC} \left(\frac{\eta P_{\rm inc}}{h\nu} \right) e \tag{1}$$

where $P_{\rm inc}$ is the radiation power incident on the detector, $P_{\rm inc}/h\nu$ is the incident photon flux, $P_{\rm abs} = \eta P_{\rm inc}$ is the absorbed power with η ($<$1) being the quantum efficiency of

Manuscript received March 9, 2010; revised April 12, 2010; accepted April 12, 2010. Date of publication June 1, 2010; date of current version February 4, 2011. This work was supported by the Japanese Science and Technology Agency through the Core Research for Evolution Science and Technology Project.

The author is with the Department of Basic Science, University of Tokyo, Tokyo 153-8902, Japan (e-mail: skomiyama@thz.c.u-tokyo.ac.jp).

Color versions of one or more of the figures in this paper are available online at http://ieeexplore.ieee.org.

Digital Object Identifier 10.1109/JSTQE.2010.2048893

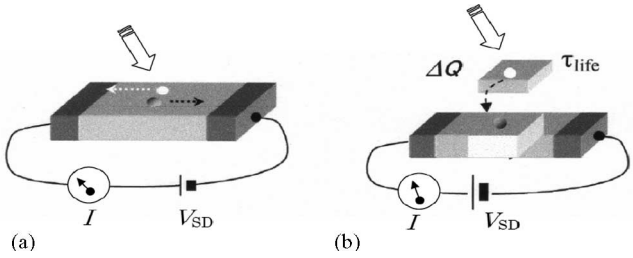

Fig. 1. Schematic representation of the detection mechanism. (a) Conventional scheme. (b) Novel scheme.

photon absorption, and $G_{\rm PC}$ is the number of electrons carried from the source to the drain per one absorbed photon, referred to as the photoconductive gain [19]. The photocurrent induced by a unit incident power

$$R_{\rm current} \equiv \frac{I_{\rm sig}}{P_{\rm inc}} = G_{\rm PC}\left(\frac{\eta}{h\nu}\right)e \tag{2}$$

is called the current responsivity. In conventional photoconductive detectors, as shown in Fig. 1(a), one electron is excited by one photon and is at best carried to the drain. Usually, it follows that $G_{\rm PC} < 1$ and the current responsivity is thereby upperbound by $R_{\rm current} = e/h\nu$, which is ca. 8 A/W for $h\nu =$ 124 meV ($\lambda = 10$ μm). This imposes a stringent restriction to the sensitivity of conventional detectors.

A series of THz singe-photon detectors, described in this article, adopt a different detection scheme, as shown in Fig. 1(b). A photon is absorbed by an isolated small semiconductor island and an electron tunnels out of the island. Losing one electron, the island is positively charged up by unit charge +e (hereafter referred to as a "hole"). The excited electron outside the island is separated from the hole by a potential barrier, yielding a long-recombination lifetime $\tau_{\rm life}$ of the excited electron hole pair. A charge-sensitive device is placed nearby the island to detect the charging-up of the island. If the current through the device changes by ΔI_e due to +e, one photon absorption drives $\tau_{\rm life}\Delta I_e/e$ electrons from the source to the drain, so that

$$G_{\rm PC} = \frac{\tau_{\rm life}\Delta I_e}{e}. \tag{3}$$

In the detectors described in this paper, $G_{\rm PC} = 10^5$–10^{12} are typically achieved, which are comparable to the carrier multiplication ratio of conventional photomultiplier tubes. It immediately leads to an incredibly large $R_{\rm current}$, ranging from 10^6 to 10^{10} A/W.

It is important in the scheme of Fig. 1(b) that a charging energy

$$\varepsilon_{\rm ch} = \frac{Ne^2}{C} \tag{4}$$

is stored by the charging up of the island (+e), where C is the capacitance of the island with respect to the environment, and N is a number of excited charges stored in the isolated island, which can be unity or more depending on the architecture.

The scheme of Fig. 1(b) is implemented in GaAs/AlGaAs heterostructure crystals. The resultant detectors are divided into two groups. Section III describes the first group, called the QD detector. The wavelength range is so far $\lambda =$ 140–210 μm and $\lambda \approx 600$ μm. Section IV describes the second group, called the CSIP. The detection wavelength range is so far limited to $\lambda \approx$ 12–29 μm, and an attempt of expanding the range is now in progress.

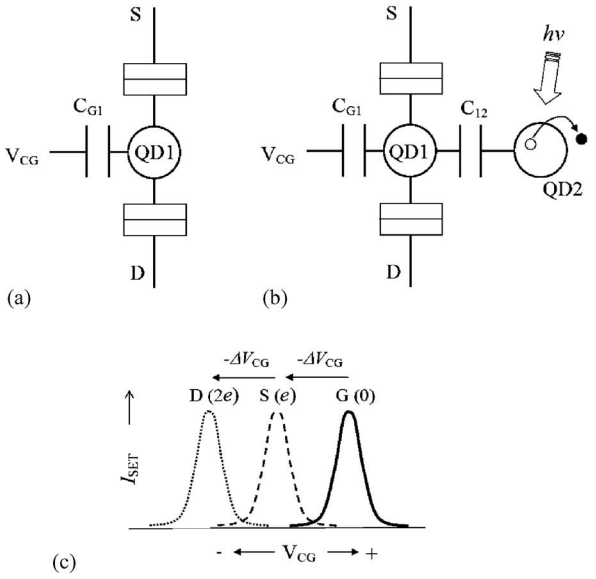

Fig. 2. Schematic representation of (a) SET and (b) QD detector. (c) Shift of the conductance resonance.

In the measurements described shortly, detectors are placed in a closed metal can at the temperature equal to that of the detector ($T =$ 70 mK to 4.2 K). The detectors are thus protected from warm thermal radiation.

III. QD Detectors

An excited charge on a QD is sensed by a SET. An SET is known as an extremely low-noise electrical device with extraordinarily high sensitivity to the electrostatic/electromagnetic environment [20], [21]. It consists of a small conductive island weakly tunnel coupled to two reservoirs (source and drain), as schematically shown in Fig. 2(a). The source–drain tunnel current through the SET I_{DS} is finite only when the electrochemical potential of the island (QD1) aligns with the Fermi level of the reservoirs (S and D). The control gate bias voltage $V_{\rm CG}$ is used to tune the electrochemical potential of the QD, so that I_{DS} exhibits a sharp "conductance resonance" as $V_{\rm CG}$ is scanned, as shown with a solid line in Fig. 2(c).

QD detectors are constructed by adding another QD (QD2) to the SET, as shown in Fig. 2(b). When a unit charge +e is photoexcited in QD2, the electrochemical potential of QD1 changes ($\Delta\mu_1$) through the capacitive coupling C_{12} between QD1 and QD2. The conductance resonance peak thereby shifts to lower the value of $V_{\rm CG}$ by an amplitude $\Delta V_{\rm CG}$ proportional to $\Delta\mu_1$, as shown with the broken line S(e). If two unit charges are excited in QD2, the shift is doubled, as shown with the dotted line D(2e).

The single-electron charging energy is defined as

$$\varepsilon_{\rm ch1} = \frac{e^2}{C_i} \tag{5}$$

for QDi ($i = 1, 2$), where C_i is the total capacitance of QDi against the environment [20].

Three conditions are necessary for the QD detectors. First, the number of electrons in each QD has to be well defined, so that

$$k_B T \ll \varepsilon_{\rm ch1}, \qquad i = 1, 2. \tag{6}$$

Second, the source–drain bias voltage V_{SD} should be so small that an excess electron is not injected to QD1

$$eV_{SD} \ll \varepsilon_{\rm ch1} \tag{7}$$

Third, a THz photon is able to add (remove) one electron to (from) QD2, namely

$$\varepsilon_{\rm ch2} < h\nu. \tag{8}$$

An implicit condition of the SET is that the tunnel coupling of QD1 to the reservoirs (source and rain) be so weak that the conductance at resonance $g_{\rm SET}$ is smaller than the quantized conductance value, namely

$$g_{\rm SET} \ll \frac{2e^2}{h} = 1/(12.6\ {\rm k}\Omega). \tag{9}$$

The source–drain current through the SET $I_{SD} = g_{\rm SET} V_{SD}$ is limited through relations (7) and (9) to

$$I_{SD} \ll \left(\frac{2e}{h}\right) \varepsilon_{\rm ch1}. \tag{10}$$

From these relations, realistic experimental conditions are such that $T \leq 400$ mK, $V_{SD} \leq 40$ μV, $g_{\rm SET} \leq 1/200$ kΩ, and $I_{SD} \leq 200$ pA. Single-photon absorption can completely turns on or off the SET conductance $\Delta I_e = I_{SD} = 200$ pA in (3), as will be shown later. This implies a huge photoconductive gain of $G_{\rm PC} \sim 10^6$ if $\tau_{\rm life} = 1$ ms. Since the single-photon induced signal is large, the single event of photon absorption can be readily recorded with a conventional current (or voltage) amplifier operating at room temperature. It should also be noted that $\Delta\mu_1 \ll h\nu$ in general.

The photon-detection scheme here should be distinguished from the well-known "photon-assisted tunneling" of SET, in which a photon of $h\nu$ is absorbed by an SET, yielding a shifted conductance resonance at $\Delta V_{\rm CG} \propto \Delta\mu_1 = h\nu$ [20]. In this effect, one photon leads to one electron transfer, so that the sensitivity is strictly limited as in conventional detectors ($G_{\rm PC} = 1$). Frequency tunability ($\Delta V_{\rm CG} \propto \Delta\mu_1 = h\nu$), however, may be an attractive feature [23]. Photon-assisted tunneling in normal-metal superconductor normal-metal SETs was suggested to yield $G_{\rm PC} \approx 100$ for microwave photons [24]. Application of this effect to high-sensitivity detection, however, has not been explored.

A. Double QD Detector

The most straightforward realization of the QD detector is a double QD (DQD) single-photon detector implemented in a GaAs/Al$_x$Ga$_{1-x}$As heterostructure crystal [7], [22]. An example is shown in Fig. 3(a), where the regions indicated by light color are metal gates [cross gate (CG), FG, barrier gate (BG), and antenna) deposited on top of the crystal surface. A

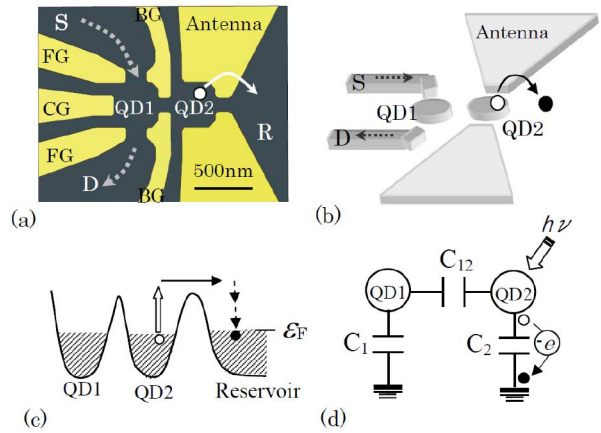

Fig. 3. DQD detector [7]. (a) Top view. (b) Schematic representation including antennas. (c) Photo-induced ionization of QD2. (d) Equivalent capacitance network.

heterointerface is located at about 100 nm below the crystal surface, where a high-mobility 10-nm-thick 2DEG layer with an electron sheet density of $n_s \approx 3 \times 10^{15}$ m^{-2} is formed. By negatively biasing the gates, the 2DEG is depleted from the regions below the gates, forming an SET (QD1) coupled with QD2. The electrical diameter of each QD is $D \approx 0.3$ μm, and is far smaller than the wavelength. Two electrodes defining QD2 extend over 0.1 mm, forming a planar dipole antenna to couple incident radiation with QD2, as schematically shown in Fig. 3(b). The mechanism of photon absorption is Kohn-mode plasma resonance [22], [25], in which collective oscillation of electrons in the confining potential of QD2 is excited.

In the detection experiment [22], cyclotron emission from a high-mobility GaAs/Al$_x$Ga$_{1-x}$As Hall bar device at $T = 2$ K is used as a tunable monochromatic radiation source, where narrow cyclotron emission line is tuned magnetically over $\nu = 70$ GHz to 2 THz. The radiation is guided through a cold 3.3 mmϕ metal light pipe (cutoff frequency at $\nu_c = 65$ GHz) and introduced into the copper shield box of the detector through silicon filters and black-polyethylene filters.

When an incident photon is absorbed in QD2, the collective oscillation energy $\varepsilon = h\nu$ is rapidly transformed via electron–electron interaction into the single-particle kinetic energy. As illustrated in Fig. 3(c), the excited single electron in turn escapes from QD2 to the electron reservoir R, where it rapidly releases its excess energy. Once the electron relaxes to the Fermi level, E_F, the potential barrier separating QD2 from R prevents the electron from returning to QD2. This leads to a long lifetime $\tau_{\rm life}$ (reaching 100 s) of the ionized state of QD2. In effect, one-photon absorption causes one electron to move from QD2 to the reservoir, as schematically shown in Fig. 3(d): the number of electrons on QD2 is reduced by 1, namely, $N_2 \rightarrow N_2 - 1$ upon the event of one photon absorption. An approximate expression [7], [22]

$$\Delta\mu_1 \approx -\left(\frac{C_{12}}{C_2}\right) \varepsilon_{\rm ch1} \tag{11}$$

is derived for the induced electrochemical potential change of QD1 through a simple analysis of the capacitance network, as

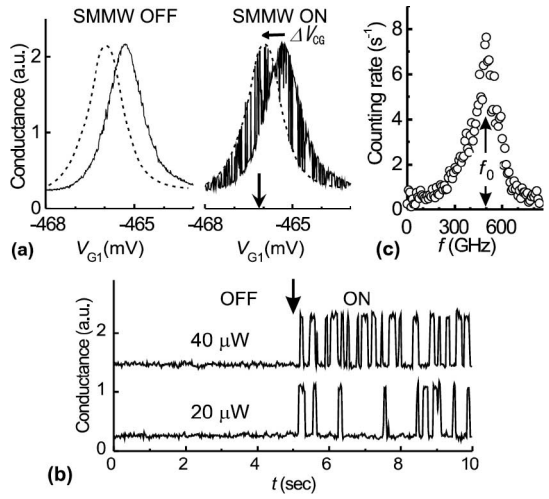

Fig. 4. DQD detector [7]. (a) Conductance peak obtained with (right) and without (left) illumination of 0.5 THz waves. Dashed and solid lines represent states with the number of electrons on QD2 differing by one. (b) Time traces of conductance showing photon counting. (c) Excitation spectrum in terms of the photon-count rate.

shown in Fig. 3(d), where $C_{12} \ll C_1, C_2 (C_{12}/C_2 \approx 0.05)$ in the experiments. The change $\Delta\mu_1$ in (11) causes the conductance resonance peak to shift toward the negative $V_{\rm CG}$ direction as has been described in Fig. 2(c).

The experimental data, as shown in Fig. 4, are taken at $T =$ 70 mK by using a 3He–4He dilution refrigerator. The two conductance resonance lines in the left panel of Fig. 4(a) are taken in the dark condition: the solid line and the broken line display the two experimental curves for which the number of electrons in QD2 differs by one to each other (N_2 and $N_2 - 1$). The two resonance lines are not completely separated because the capacitive coupling between QD1 and QD2 in the geometry of lateral double QDs is small ($C_{12}/C_2 \ll 1$) and $\Delta\mu_1$ is small. The experimental trace in the right panel is taken with extremely weak illumination. The trace exhibits switching between the states of N_2 and $N_2 - 1$, reflecting individual events of electron excitation due to photon absorption and recombination. When the gate bias voltage ($V_{\rm CG}$) is fixed at the position marked by the arrow in Fig. 4(a), telegraph-like switching shows up in the time trace, as shown in Fig. 4(b), for tow levels of radiation intensity. The radiation power incident on the detector is on the order of 10^{-18} W. Note that each switching corresponds to the absorption event of a single photon but not of more-than-one photons: this is because the experimentally found amplitude of the conductance peak shift (or $\Delta\mu_1$) exactly agrees to the value expected from the unit charge (+e) change in QD2.

The photon count rate shows distinct resonance peak at $\nu \approx$ 0.5 THz ($\lambda \approx 600$ μm, $h\nu \approx 2$ meV, $\omega \approx 17$ cm^{-1}), as shown in Fig. 4(c). This spectral response is ascribed to the Kohn-mode plasma resonance of QD2 [25]. The spectral region is expected to shift in a range $\nu = 0.4$–0.6 THz ($\lambda = 500$–750 μm, $h\nu =$ 1.6–2.4 meV) when the dot size and the sheet electron density are varied.

The minimum detectable photon flux is limited by the dark switching of the detector, the rate of which is minimized to $\Gamma \approx 0.01$/s at an optimum condition of the BG bias voltage at $T = 70$ mK. This implies that one photon in a time span of 100 s can be distinguished. The NEP resulting from this extraordinary sensitivity will be discussed in Section V.

The speed of detection can be influenced both by the instrumental time constant τ_D and the recombination lifetime of excitation $\tau_{\rm life}$. Namely, the QD detector is insensitive after a photon has been counted. This dead time lasts until the electron–hole pair disappears via recombination. Since this resetting time is $\tau_{\rm life}$, the maximum rate of photon counting is given by $\min(1/\tau_{\rm life}, 1/\tau_D)$. Actually, however, the recombination lifetime $\tau_{\rm life}$ can be made arbitrarily short by adjusting the bias condition of BG. The maximum rate is hence determined practically by the instrumental time constant τ_D. It is $\tau_D \approx 1$ ms, when a commercial current preamplifier operating at room temperature is used. As demonstrated by Ikushima *et al.* [12]–[14], it can be reduced to $\tau_D \approx 20$ μs if a voltage preamplifier (working at room temperature) is used and the SET current is measured through the voltage drop across a low-temperature series resistance (40 kΩ). It will be possible to realize $\tau_D < 1$ μs if a low-temperature RF-SET is applied [26], [27]. The intrinsic speed limit of SET is supposed to be on the order of $\tau_D = 1$ ns. The dynamic range of detection is hence 10^5–10^6, when the preamplifier is placed at room temperature and will be expanded to 10^8 if low-temperature RF-SET is applied.

B. Single QD Detector

Historically, a single QD (SQD) detector, as shown in Fig. 5, has been first developed [6], [22], [25], [28]. The detector utilizes cyclotron resonance excitation in magnetic fields. The devices are fabricated in GaAs/AlGaAs single heterostructure crystals similarly to DQD detectors. The metal gates forming an SET [the left panel of Fig. 5(a)] extend to the opposite directions, serving as a bowtie antenna [the right panel of Fig. 5(a)] that couples incident radiation to the QD.

Magnetic fields are applied normal to the plane of the QD, quantizing the energy state of electrons in the QD into discrete Landau levels (LLs), as schematically shown in Fig. 5(b). Each orbital LL splits into opposite spin states, but the spin splitting is ignored in the discussion shortly. In an appropriate range of magnetic field strength, the lowest LL (LL0) is filled with electrons, but the first excited LL (LL1) is occupied with only a small number of electrons, as shown in Fig. 5(b).

Mechanically, the dot is a SQD. Effectively, however, it is electrically split into the metallic "outer ring" (LL0) and the metallic "inner core" (LL1), as shown in Fig. 5(c). These two regions are spatially separated to each other, and in effect, function as capacitively coupled two separated QDs, QD1 (LL0) and QD2 (LL1), as schematically illustrated in the upper panel of Fig. 5(d).

When a THz photon is absorbed by the QD upon cyclotron resonance, the excited electron and the hole rapidly give up their excess energy within the QD, relaxing to the inner core and the outer ring at the Fermi level, as schematically illustrated in Fig. 5(b). It follows that the inner core and the outer ring are

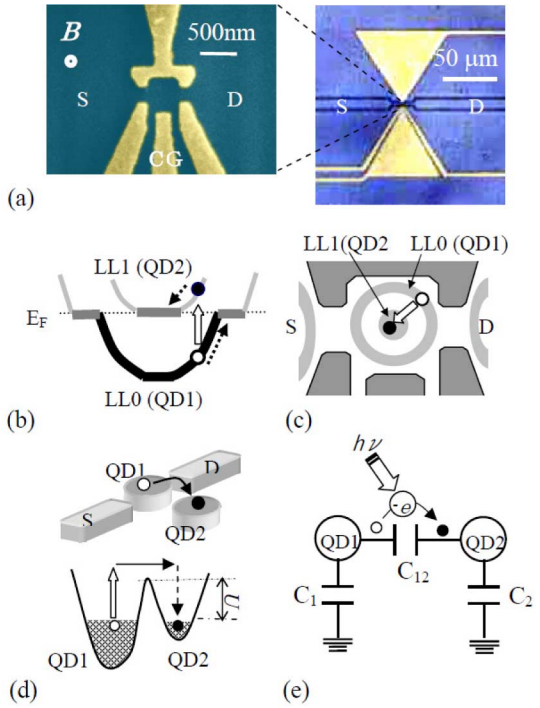

Fig. 5. SQD detector [6]. (a) Closed-up top view on the left, bird view on the right. (b) Landau-level energy diagram. (c) Schematic representation of polarized Landau levels. (d) Equivalent double QD structure (upper panel) and photo-induced inter QD polarization (lower panel). (e) Equivalent capacitance network.

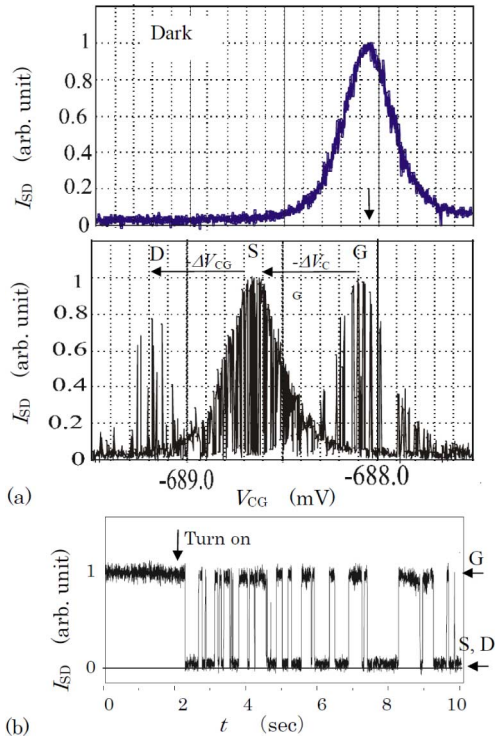

Fig. 6. SQD detector [6]. (a) Conductance peak without (upper panel) and with (lower panel) THz illumination. (b) Photon-counting signal in time trace of conductance.

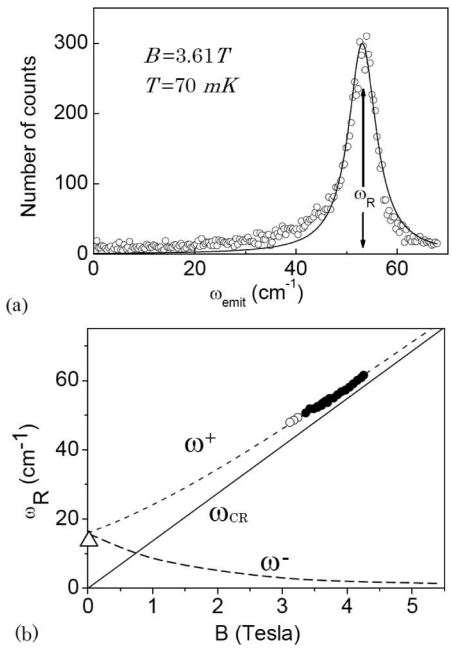

Fig. 7. SQD detector. (a) Excitation spectrum in terms of the photon-count rate [6]. (b) Resonance peak frequency against magnetic field [25].

charged by $-$e and $+$e, respectively, which is equivalent to the move of one electron from QD1 to QD2, as shown in Fig. 5(d) and (e). The induced change in the electrochemical potential of QD1 (outer ring) is approximately given by [6], [28]

$$\Delta\mu_1 \approx -\left(\frac{C_2}{C_{12}}\right)\varepsilon_{\mathrm{ch1}} \tag{12}$$

where in the experiment $C_{12} \gg C_1, C_2 (C_2/C_{12} \approx 0.15)$ hold in the capacitance network of Fig. 5(e).

Detection measurements are made by using a tunable cyclotron emission from a GaAs/AlGaAs Hall bar similar to the measurements of DQD detectors. Fig. 6(a) compare the conductance resonance curves with (lower panel) and without (upper panel) THz illumination. Since $\Delta\mu_1$ in (12) is relatively large, the ground-state (G) and the excited-state (S) conductance peaks are largely separated and single photons completely turn on or off the SET conductance. Telegraph-like switching between the nonexcited (G) and the excited state (S) is obtained when the gate bias voltage (V_{CG}) is fixed at the peak position of the ground-state conductance peak as marked by the arrow in the upper panel of Fig. 6(a).

The spectral band of response shows a narrow resonance, as shown in Fig. 7(a), and is tuned by applying different magnetic fields to the QD, as shown in Fig. 7(b). Strictly, the response is not exactly at the cyclotron resonance frequency $\omega_{\mathrm{CR}} = eB/m^*(m^* = 0/067\ \mathrm{m_o}$: the effective mass of conduction electrons in GaAs), but is shifted slightly due to coupling with Kohn plasma resonance $\omega_0 = 16\ \mathrm{cm}^{-1}$ of the QD. The coupling leads to the upper branch ω^+ of the magnetoplasma resonance [25]

$$\omega^{\pm} = \sqrt{\left(\frac{\omega_{\mathrm{CR}}}{2}\right)^2 + \omega_0^2} \pm \left(\frac{\omega_{\mathrm{CR}}}{2}\right) \tag{13}$$

which agrees very well to the experimental values, as demonstrated in Fig. 7(b). We should note that $\omega_0 = 16\ \mathrm{cm}^{-1}$ is

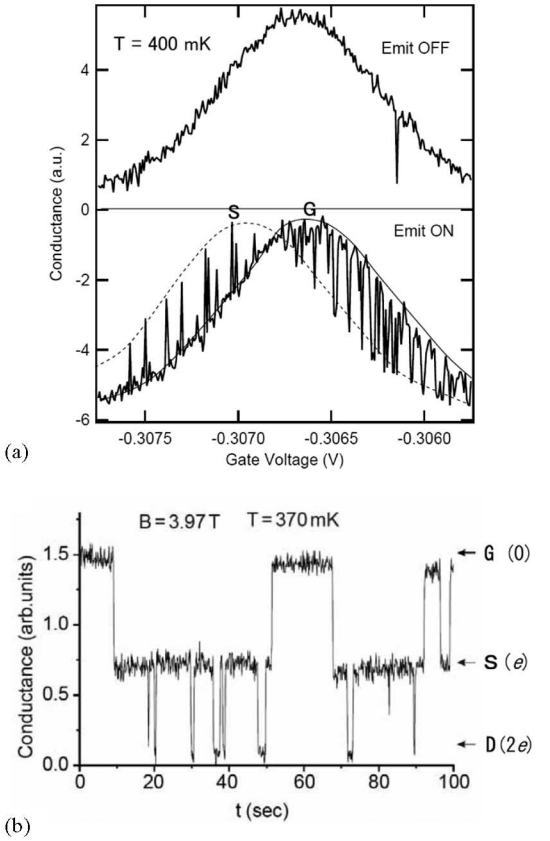

Fig. 8. SQD detector [22]. (a) Conductance peat at $T = 400$ mK. (b) Telegraph switching at $T = 370$ mK.

consistent with the detection frequency of the DQD detector [Fig. 4(c)]. Photon signal is not seen in the lower (edge-magnetoplasma) branch ω^- in Fig. 7 (a) and (b). This is because this mode does not polarize QD, and the SET conductance is insensitive to it.

The magnetic field range where photons are counted is $B = 3.1$–4.2 T ($\omega = 48$–$62\ \mathrm{cm}^{-1}$, $\nu = 1.44$–1.87 THz) in Fig. 7(b), which is determined by the sheet electron density $n_s = 2.4 \times 10^{15}\ \mathrm{m}^{-2}$ of the device. Since the magnetic field range is nearly proportional to n_s, SQD detectors may be appropriately designed for a range of $B = 1.3$–6.1 T ($\omega = 26$–$86\ \mathrm{cm}^{-1}$, $\nu = 0.8$–2.6 THz) by choosing crystals with $n_s = (1.0$–$3.5) \times 10^{15}\ \mathrm{m}^{-2}$.

The dark switching rate is extremely low such that $\Gamma < 0.001$/s in appropriate magnetic fields at $T = 70$ mK. Resulting NEP is hence even smaller than that of the DQD detectors, as will be discussed in Section V.

Fig. 8 displays a few effects of elevating temperature. At $T \approx 400$ mK, the conductance resonance line significantly broadens but the photon-counting signal is still clearly visible, as shown in Fig. 8(a), where the current is recorded at a detection speed of $\tau_D \approx 20\ \mu$s by using a low-T resistor close to the SET.

When the incident photon flux increases so that the photon arrival rate exceeds the recombination rate of photo-excited electron–hole pairs, two electrons (holes) are accumulated QD2 (QD1). Such doubly charged state, D(2e), as shown in Fig. 2(c),

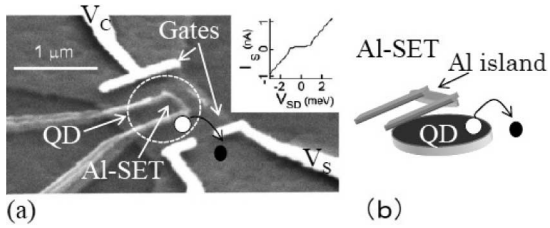

Fig. 9. Al-SET/QD detector [8]. (a) SEM image. (b) Schematic representation.

is visible in Fig. 6(a) as several conductance spikes occurring at the position shifted twice as large as that of the singly charged state, S(e). At $T = 70$ mK, the doubly charged state D(2e) should be equally present. However, the resulting signal is invisible in the telegraph switching in Fig. 6(b), because both of S(e) and D(2e) completely turn off the conductance. At elevated T, S(e)-state does not completely turn off the SET conductance but D(2e)-state does. It follows that the two excited states of the QD are distinguished, as shown in Fig. 8(b) [22].

The recombination lifetime $\tau_{\mathrm{life}}(\mathrm{S} \rightarrow \mathrm{G})$ is substantially longer than that of the QDD detectors, because spin-flip process is involved [22]. The lifetime reaches $\tau_{\mathrm{life}} \approx 1000$ s at 4.2 T (the highest allowable magnetic field). As T is elevated up to 400 mK, τ_{life} is reduced by a factor around 300. Furthermore, τ_{life} for $D \rightarrow S$ is shorter than that for $S \rightarrow G$ roughly by a factor about $\sim$50. Similarly to the case of DQD detector, τ_{life} can be made so small that the photon-counting rate is actually determined by the instrumental detection speed $1/\tau_D$. The detection speed ranges from $\tau_D = 1$ ms to less than 1 μs, as described for the DQD detector. Since $\Gamma = 0.001$/s, the dynamic range of detection is even wider than the DQD detector by a factor of ca.10.

The SQD detectors ($T = 300$ mK) have been successfully applied by Ikushima *et al*. for the construction of a photon-counting scanning passive THz microscope [12], [13]. The microscope was used to image extremely weak THz radiation emitted by nonequilibrium electrons in quantum Hall electron systems at $T = 4.2$ K with a subwavelength resolution (50 μm) via photon-counting technique. More recently, on-chip manipulation of THz photons has been demonstrated [14], i.e., generation, propagation, and detection of single THz photons have been completed on-chip, where THz photons generated by a quantum Hall Corbino device are coupled into a coplanar waveguide, transmitted through the line and finally fed to a SQD detector. In this experiment, THz photons are manipulated all the way in near-field mode localized in super subwavelength narrow regions. This may be a first step approaching an integrated THz-photon lab or spectrometer on a chip.

C. Al-SET/QD Detector

The photon detector is constructed also by placing aluminum—SET on top of a semiconductor QD, as shown in Fig. 9 [8]. This type of detectors has been extensively studied at the group of Royal Holloway University of London [29]–[32]. The device structure is similar to the one studied by Lu *et al.* [33] and Chen *et al.* [34]. An Al-SET consists of a small Al island

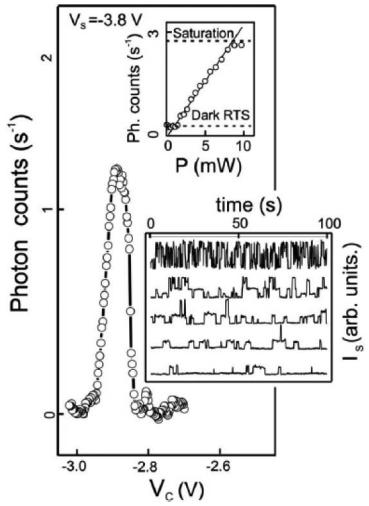

Fig. 10. Al-SET/QD detector [8]. Photon-count rate against V_c. Lower inset displays telegraph-like photon-counting signal.

connected to Al leads through Al oxide tunnel junctions [35]. The QD is formed in a GaAs/AlGaAs heterostructure crystal. Detection scheme is similar to that of DQD detectors: an excited electron escapes from the semiconductor QD, and the induced charge on the QD is sensed by the Al-SET. Advantage of this detector is a stronger capacitive coupling (C_{12}) between the AL-SET and the QD. Fig. 10 shows the induced telegraph-like switching of the current through the AL-SET ($T = 0.3$ K), when the device is illuminated with an extremely weak thermal radiation from a chip-resistor heated in a cryogenic condition. Although accurate excitation spectrum has not been studied, the excitation is supposed to be via Kohn-mode plasma resonance as in the DQD detector ($\nu < 500$ GHz). Al-SET/QD detector does not require accurate adjustment of potential barriers. This, together with the fact that Al-SETs can work at elevated temperatures, makes the AL-SET/QD detector potentially an attractive THz-photon counting sensor.

D. Miscellaneous

The QD detectors aforementioned require ultralow temperatures (<1 K). SETs formed by much smaller 1-D carbon nanotubes (CNT) [36] can be operated at higher temperatures providing attractive candidates of charge sensors. A CNT SET formed on top of GaAs/AlGaAs heterostructure with a 2DEG layer is shown to exhibit sensitive response to THz radiation in magnetic fields at $T = 2.5$ K [37]. In view of application, however, significant elaboration of device fabrication technique will be necessary.

The demand for ultralow temperatures is substantially relaxed also by replacing the SET with a quantum point contact (QPC), as shown in Fig. 11. A QPC is a saddle point potential barrier, controlling the electron conduction through the narrow constriction. The conduction through a QPC is known to be sensitive to a charge on a nearby QD. Pelling *et al.* studied a QPC coupled to a QD in a GaAs/AlGaAs heterosturcure and found high-sensitive response to THz waves at $T = 1.5$ K [38].

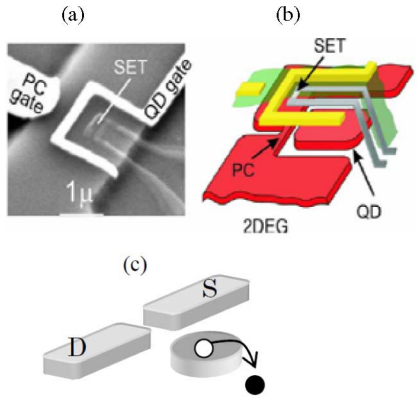

Fig. 11. Point contact detector [37]. (a) SEM image. Schematic representations of (b) device and (c) mechanism.

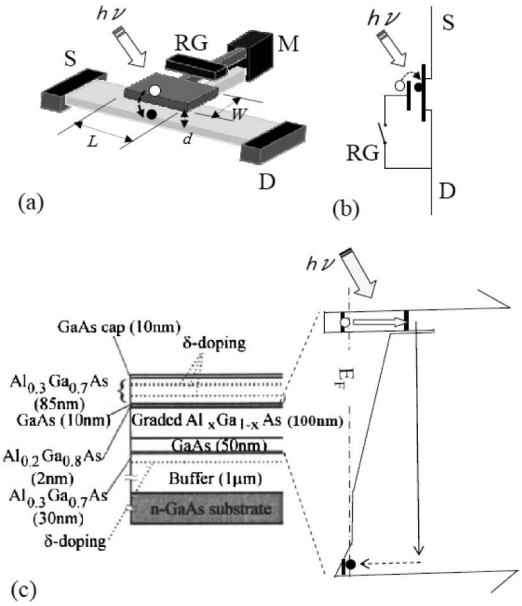

Fig. 12. CSIP [9]. (a) Schematic representation of the device. (b) Equivalent circuit. (c) Heterostructure with DQWs (left) and the conduction-band energy diagram.

IV. Charge-Sensitive IR Phototransistor

Distinct advantage of QD detectors described in Section III is the outstanding sensitivity. The application of these detectors, however, might be restricted because 1) ultralow temperatures (<1 K) are necessary and 2) a certain device fabrication technique is required. The spectral range of detection may be also limited to relatively long wavelengths if the excitation mechanism relies on Kohn-mode plasma resonance and magneto-plasma resonance.

An attractive solution to the problem is given by the photosensitive field-effect transistor fabricated in a double-quantum-well (DQW) structure, called a CSIP [9], [39]–[43]. As shown in Fig. 12(a)–(c), an electron in an isolated island of the upper QW is photo-excited via intersubband transition, tunnels out of the QW and moves to the lower QW. Missing one electron, the isolated QW island is positively charged up by +e. The resultant charge accumulated on the isolated upper QW

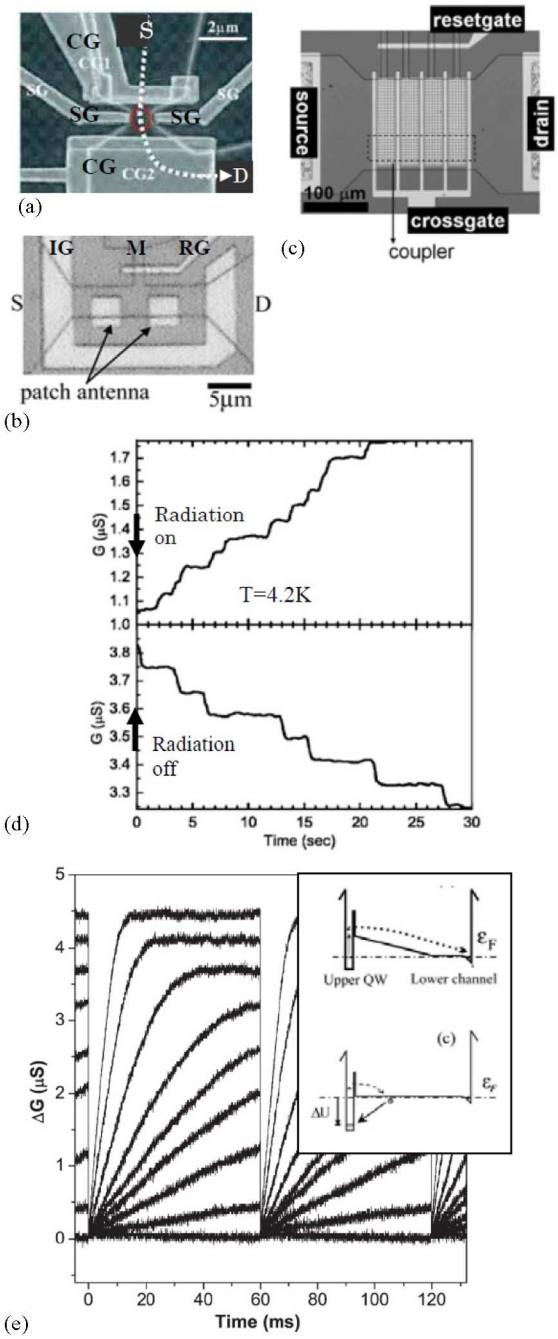

Fig. 13. CSIP detectors with $L \times W =$ (a) 1.5×0.8 μm^2 [39], (b) 16×4 μm^2 [40], (c) 130×120 μm^2 [42]. (d) Photo-induced conductance $G = I_{\rm sig}/V_{SD}$ in device (a) [39]. (e) Time traces of $\Delta G = I_{\rm sig}/V_{SD}$ at different radiation intensities, obtained in reset operation [40]. The inset elucidates the mechanism of signal saturation.

island is sensed by the conduction channel in the lower QW. The device is implemented in a GaAs/AlGaAs modulation-doped heterostructure crystal containing two 2DEG layers. The device can be designed in a wide range of scale size: for instance, the photoactive region (the area of the upper QW isolated island) in devices shown in Fig. 13(a)–(c) ranges from $L \times W \approx 1.5 \times 0.8$ μm^2 [Fig. 13(a)] [40], 16×4 μm^2 [Fig. 13(b)] [41] to 130×120 μm^2 [Fig. 13(c)] [43] for a wavelength of 15 μm. The isolated island of the upper QW is formed by negatively biasing isolation gates or CG and a reset gate (RG) in respective devices, as shown in Fig. 13(a)–(c), and it serves as a photosensitive floating gate for the lower conducting channel.

In each device, a metallic photocoupler is deposited on top of the isolated QW island, so that alternating electric fields normal to the plane of the QW are generated against normally incident radiation.

A. Mechanism of Amplification

When one photon is absorbed in the upper QW island and a photo-excited electron reaches the lower conducting channel, it increases the conductance of the lower channel but rapidly leaves the channel after the transit time

$$\tau_{\rm trans} = \frac{L}{\mu E} \tag{14}$$

where L is the length of the isolated upper QW island, μ is the electron mobility of the lower conducting channel and

$$E = \frac{\alpha V_{SD}}{L} \tag{15}$$

is the electric field in the channel, where V_{SD} is the source–drain bias voltage and α (not very far from unity) is a geometrical factor of the device considering voltage drops in the photoinactive regions. The transit time is as short as $\tau_{\rm trans} = 20$ ps in a typical experimental condition of $L = 2$ μm, $\mu = 10$ m^2/Vs, $V_{SD} =$ 20 mV, and $\alpha = 1$.

A large photoconductive gain results from the current induced after the excited electron has left the channel. Namely, so long as the upper QW island is kept charged (+e), another electron is introduced to the lower channel as soon as the excited electron leaves the channel. Hence, the number of electrons in the lower channel is kept larger by 1. This is because the isolated upper QW island forms a parallel plate capacitor with the lower conducting channel. When small parasitic capacitance of the isolated upper QW island is ignored, an opposite charge of the same amplitude (−e) is induced in the lower conducting channel. Hence, the current through the conducting channel increases by the amount of one additional electron

$$\Delta I_e = \frac{(\alpha e \mu E)}{L} = \frac{\left(\alpha^2 e \mu V_{SD}\right)}{L^2} = \frac{\alpha e}{\tau_{\rm trans}} \tag{16}$$

and the increment is maintained until +e disappears due to recombination. This current increment is large enough to be detected if the 2DEG conducting channel is of typical, and L is relatively small, say, $L < 15$ μm. The photoconductive gain is given by

$$G_{\rm PC} = \frac{\tau_{\rm life} \Delta I_e}{e} = \frac{\alpha \tau_{\rm life}}{\tau_{\rm trans}}. \tag{17}$$

Since $eV_{SD} < h\nu$ is required, ΔI_e is limited by

$$\Delta I_e < \frac{\mu h \nu}{L^2}. \tag{18}$$

Remarkable advantage of the CSIP is that the recombination lifetime $\tau_{\rm life}$ of photo-induced charge is extremely long, say, more than an hour. It follows that the photon-counting signal

manifests itself as a stepwise current increase with the step amplitude of ΔI_e. This is demonstrated in Fig. 13(d), where a time trace of the conductance $G = I/V_{SD}$ in the CSIP for $\lambda = 14.7\ \mu$m with $L \times W \approx 1.3 \times 0.8\ \mu\text{m}^2$ and $\mu = 7.5\ \text{m}^2/\text{Vs}$ [see Fig. 13(a)] is displayed [40]. The data are taken with $V_{SD} = 2$ mV at $T = 4.2$ K. The conductance step $\Delta G \approx 0.05\ \mu$S ($\Delta I_e \approx 100$ pA) agrees with the value predicted by (16). The time trace displayed in the lower panel of Fig. 13(b) shows that the piled up charge on the isolated QW island slowly diminishes step wise by e when the radiation is turned off. Also in a larger CSIP device of $L \times W \approx 16 \times 4\ \mu\text{m}^2$ and $\mu = 0.43\ \text{m}^2/\text{Vs}$ [see Fig. 13(b)], step-wise single-photon signal can be recognized ($\Delta I_e = 3$ pA with $V_{SD} = 10$ mV) [41].

Under constant radiation, the photocurrent increases at an average rate of

$$\frac{\partial I}{\partial t} = \eta \Phi_{\text{inc}} \Delta I_e \tag{19}$$

where Φ_{inc} is the photon flux incident on the photoactive area and the quantum efficiency

$$\eta = \eta_1 \eta_2 \tag{20}$$

is the multiple of the fraction η_1 of incident photons that are absorbed to excite electrons via intersubband transition in the upper QW, and the fraction η_2 of excited electrons that reach the lower 2DEG layer.

The rate of photocurrent increase is proportional to the incident radiation intensity. As shown in Fig. 13(e) for different radiation intensities [41], the increase levels off when the charge accumulation reaches a given level $Q_{\text{sat}} \approx (C/e)h\nu$, where the electrostatic potential difference $\Delta U = eQ/C$ with $C = \varepsilon\, LW/d$ (ε: the dielectric constant of GaAs) between the upper QW and the lower 2DEG approaches the photon energy $h\nu$, as elucidated in Fig. 13(e) (inset).

B. Reset Operation

For use as a detector, the accumulated charge is released to the reservoir by applying a brief positive pulse (e.g., +0.3 V, 1 μs) to the RG, and the CSIP is reset to the original highly sensitive state [41]. Fig. 13(e) displays photo signals in the reset operation. The reset pulse interval τ_{reset} can be chosen appropriately according to the incident radiation intensity. The overall function of CSIPSs is thus similar to that of CMOS sensors [44]. While the intrinsic recombination lifetime is practically indefinite, effective lifetime can be externally defined by the reset pulse. The recombination lifetime τ_{life} in (3) and (17) should be replaced by

$$\tau_{\text{life}} = \frac{\tau_{\text{reset}}}{2} \tag{21}$$

Typically, $G_{\text{PC}} = 10^6$–10^{10} and $R_{\text{current}} = 10^4$–$10^8$ A/W are obtained for $\tau_{\text{reset}} = 0.1$ ms to 10 s. The speed of detection is also determined by τ_{reset}. NEP of a device with $L \times W \approx 16 \times 4\ \mu\text{m}^2$ [see Fig. 13(b)] is as low as NEP $= 6.8 \times 10^{-19}\ \text{W/Hz}^{1/2}$, and even distinctly lower values are theoretically expected as discussed in the next section. It should be mentioned that photon energies are stored in the form of electrostatic energy in the capacitor, $C = \varepsilon LW/d$. Letting $Q = Ne$ be the accumulated charge at the time of reset, the stored electrostatic energy is $E_N = Q^2/(2\ C) = (Ne)^2/(2\ C)$. The "charging energy" necessary to add +e at the time of reset is $\varepsilon_{\text{ch}} = \partial E_N/\partial N = Ne^2/C$ [see (4)]. The average fraction of photon energies that is transformed to the electrostatic energy and is stored in the capacitor amounts to $E_N/(Nh\nu) = (1/2)Q/Q_{\text{sat}} \sim 0.2$.

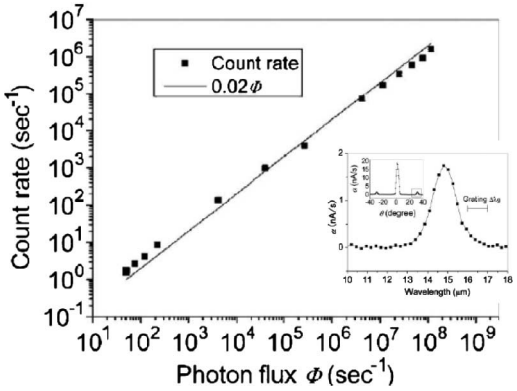

Fig. 14. Photon-count rate against incident photon rate [9]. Dynamic range of linear response is larger than 10^6. The inset shows the spectral response.

C. Characteristics

Another important characteristic of CSIP is a large dynamic range of linear response ($>10^6$), as shown in Fig. 14 [9], where normalized current signal $(\partial I/\partial t)/\Delta I_e$ is plotted against Φ. Here, absolute values of Φ are determined by the temperature of a calibrated blackbody emitter. The upperbound of the dynamic range in Fig. 14 is restricted by the maximum radiation intensity available in the experiment. A dynamic range of 10^8 may be realized without too much technological demand.

Quantum efficiency η is an important parameter for the detector. High values of η (>30%) are reported in conventional QW IR photodetectors, where photons are absorbed by more than 30 multiple QWs. High quantum efficiency is not trivial in CSIPs, where photons are absorbed by only one QW. In most experimental conditions of CSIP for $\lambda = 12$–$15\ \mu$m, the efficiency $\eta = \eta_1\eta_2$ is primarily determined by the coupling strength of electrons to the incident radiation, namely, $\eta \approx \eta_1 (\eta_2 \approx 1)$. The quantum efficiency has been experimentally studied by applying different metal photocouplers as displayed in the top panel of Fig. 15 and compared with simulation results in Fig. 15(a) and (b) [43]. In the experiments, an efficiency of $\eta \approx 7\%$ has been achieved by utilizing the surface plasmon excitation in a 2-D metal hole array (inductive metal mesh) with cross-shaped holes lining up at a lattice period of 4 μm ($\sim$ wavelength in GaAs). Other coupler geometries such as 2-D metal hole arrays with square-shaped holes, 2-D metal patch arrays (capacitive metal mesh), and patch antennas (microstrip antennas) have yielded lower values of $\eta \approx 1\%$–3% [9], [43]. The device used for Fig. 14, for instance, utilizes a patch antenna coupler yielding $\eta \approx 2\%$ [9]. Simulation calculation suggests that $\eta \approx 7\%$ is not a highest achievable value but can be improved by a factor

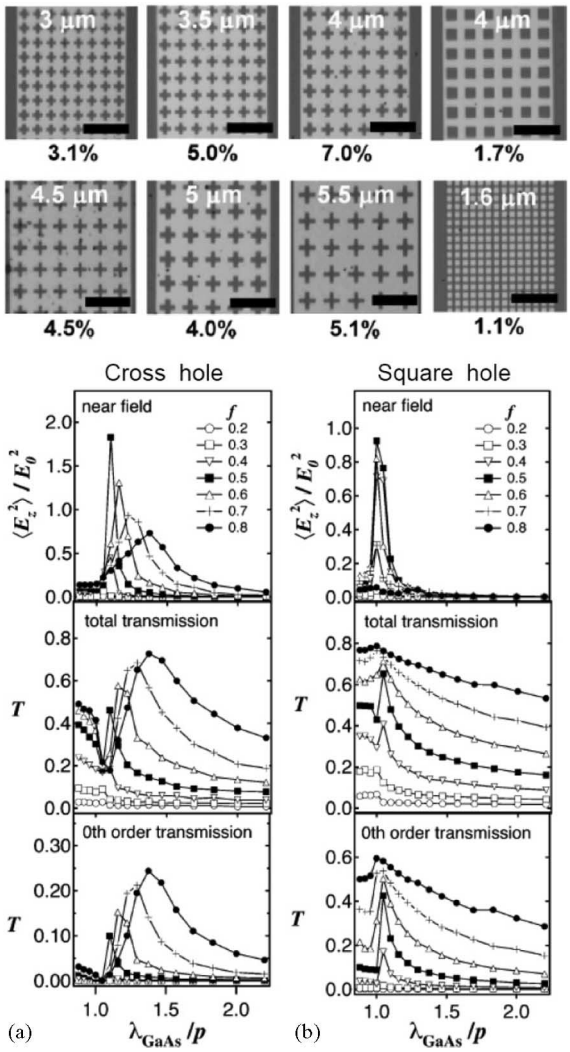

Fig. 15. Photocouplers for CSIPs ($\lambda = 15\ \mu$m) [42]. Top panel displays metal meshes studied. White and black characters indicate, respectively, the lattice period p and the experimentally derived quantum efficiency η. Results of simulation calculation are shown for (a) cross-hole arrays and (b) square-hole arrays: from the top, normalized field intensity $\langle E_z^2\rangle/\langle E_{x0}^2\rangle$, the total power transmission, and the zeroth-order transmission, against the ratio $\lambda_{\mathrm{GaAs}}/p$ with $\lambda_{\mathrm{GaAs}} = 4.3\ \mu$m. E_z is the electric field normal to the QW plane at the position of upper QW (100 nm below the surface) and E_{x0} is the electric field of incident radiation. Theoretically, $\langle E_z^2\rangle/\langle E_{x0}^2\rangle = 2$ gives roughly $\eta = 7\%$, which agrees with the experiment.

of $\sim$3 ($\eta \approx 20\%$) when a resonant cavity is formed by the metal hole array and the n-type substrate [45]. Values of the current responsivity and the NEP have been so far derived by assuming $\eta = 2\%$. The figure-of-merits of the CSIP will be improved in accord to η.

Up to the present time CSIPs have been studied primarily for wavelengths of $\lambda = 12\ \mu$m and 15 μm [see Fig. 14 (inset)]. Expansion to longer wavelengths has been attempted by modifying the design of DQW structures, and the radiations of $\lambda = 27$, 29 [46], and 45 μm [47] have been detected at $T = 4.2$ K. The detection sensitivity, however, is limited because of low-quantum efficiency ($\eta_2 \ll 1$). Efforts are being made to elaborate crystal quality and optimize the design of crystal structure as well as the device structure. A novel device design, in which excited electrons escape "laterally" through the isolation-gate induced potential barrier [48] might give a possible solution. Temperature dependence of detector performance has been studied ($\lambda = 15\ \mu$m) and the sensitivity is found to be maintained up to $\sim$25 K without substantial degradation [42]. The high temperature limit is determined by a rapid reduction in τ_{life} due to pronounced recombination by thermally activated electrons.

A marked strength of CSIP is the coexistence of the high sensitivity and an extremely large current responsivity. In addition very low output impedance $Z = \alpha L/(ne\mu W)$, typically, $Z = 10^2$–$10^4\ \Omega$ makes electrical measurements simple. Furthermore, device structure of the CSIP is simple and does not demand extensive fabrication technique. This may be beneficial for integrating large-format 2-D array by processing channel patterns and electrodes on a GaAs/AlGaAs wafer. Monolithic integration of CSIPs with GaAs LSIs may be also expected, where photosignal is easily multiplexed and buffered. It is also mentioned that InP/InGaAsP heterostructure crystals are free from oxygen-related defects and are promising host materials for the architecture of CSIPs.

Outstanding sensitivity along with ease of use makes CSIPs extremely promising detectors for versatile applications. In fact, a sensitive scanning confocal microscope for the study of thermal radiation of matters at room temperature has been developed by using CSIPs ($\lambda = 15\ \mu$m) [15]. More recently, benefiting from unparalleled sensitivity, a novel near-field scanning microscope has been successfully developed for the study of thermal radiation with superwavelength resolution (without external illumination) [16]. Extremely weak evanescent waves activated by random thermal motion of conduction electrons or thermal lattice vibrations are scattered by a tungsten probe tip controlled by atomic force microscope (AFM) near the sample surface and are guided to the CSIP. Thermally excited surface plasmons in gold stripes are imaged with a spatial resolution ca., 150 nm (λ/100). It is highly probable that the range of application will be largely expanded in the future.

V. Sensitivity

Sensitivity of the photon detectors described in this paper is discussed in terms of NEP shortly. Different definitions of NEP are occasionally applied in literatures. To avoid confusion and to make comparison with other detectors meaningful, we first pay attention to the physical implication of NEP.

The sensitivity of a given detector is expressed by the inverse of

$$\mathrm{NEP}_1 = \frac{P_{\mathrm{inc}}}{\{(S/N)\Delta f^{1/2}\}} \quad \text{or} \quad \frac{((2\Gamma)^{1/2}h\nu)}{\eta} \tag{22}$$

where the second expression refers to the photon-counting mode [22], [49]. Here, $P_{\mathrm{inc}} = \Phi_{\mathrm{inc}}h\nu = \phi A h\nu$ is the radiation power incident on the photoactive area A of the detector with ϕ the photon flux per unit area, S/N is the signal-to-noise ratio, Δf is the measurement bandwidth, and Γ is the rate of dark switching. If the detector size D is comparable to or smaller than λ, the "photoactive area A" is not a trivial quantity: The area is not

TABLE I
SENSITIVITY OF QD DETECTORS AND CSIPS IN TERMS OF NEP [W/Hz$^{1/2}$]

	QD detector (T=70mK)		CSIP (T=4.2K)	
	DQD $h\nu$=2meV	SQD $h\nu$=6meV	LxW=16x4μm^2 $h\nu$=84 meV	LxW= 1.5x0.8μ $h\nu$=84 meV
NEP_1	4.5x10^{-21}	4.3x10^{-21}	6.8x10^{-19}	-----
NEP_2	4.5x10^{-23}	4.3x10^{-23}	1.4x10^{-20}	4.0 x10^{-21}
NEP_{shot}	------	--------	2.5x10^{-21}	3.2x10^{-23}
$NEP_{Johnson}$	-------	--------	4.6 x10^{-22}	6.1x10^{-24}

NEP_1 and NEP_2 are determined by detection measurements.

determined merely by D alone but depends on the detailed distribution of materials around the detector. In such a condition, NEP_1 is difficult to determine in a straightforward way, and

$$\mathrm{NEP}_2 = \frac{P_{abc}}{\{(S/N)\,\Delta f^{1/2}\}} \text{ or } (2\Gamma)^{1/2}\,h\nu \tag{23}$$

with $P_{\mathrm{abs}} = \eta P_{\mathrm{inc}}$ provides a convenient parameter. NEP_2 represents an NEP that would be attained if the detector were ideally coupled to the radiation ($\eta = 1$). Noting $I_{\mathrm{sig}} = G_{\mathrm{PC}}(P_{\mathrm{abs}}/h\nu)e$, the first expression of (23) is rewritten as

$$\mathrm{NEP}_2 = \left(\langle I_n^2\rangle\,\Delta f\right)^{1/2}\left(\frac{h\nu}{eG_{\mathrm{PC}}}\right) \tag{24}$$

where $\langle I_n^2\rangle^{1/2}$ is the noise current in the frequency bandwidth Δf.

In true physical devices, the noise current or the dark switching rate can be affected by device-specific imperfections. NEP_1 and NEP_2 are hence device-specific parameters in general. It is therefore meaningful to ask a device-independent theoretical $\mathrm{NEP}_{\mathrm{theory}}$, which would be realized if the device is free from any imperfection. Such $\mathrm{NEP}_{\mathrm{theory}}$ can be derived by considering the noise arising from statistical fluctuations such as Johnson noise, shot noise, and thermal-fluctuation noise etc. It is self-evident that $\mathrm{NEP}_1 > \mathrm{NEP}_2 > \mathrm{NEP}_{\mathrm{teory}}$.

Values of NEP are listed in Table I for QD detectors and CSIPs. To evaluate NEP_1 and NEP_2, dark switching rate was studied experimentally. In a DQD detector ($h\nu = 2$ meV) at $T =$ 70 mK, $\Gamma \approx 0.01$ /s was found, which with (23) yields an incredible value $\mathrm{NEP}_2 = 4.5 \times 10^{-23}$ W/Hz$^{1/2}$. In a SQD detector at $T = 70$ mK, dark switching is even less frequent, for instance, it was not observed at all for 1000 s in $B = 4$ T ($h\nu = 6$ meV) [6]. The value in the table, $\mathrm{NEP}_2 = 4.3 \times 10^{-23}$ W/Hz$^{1/2}$, is obtained by assuming $\Gamma = 0.001$/s. (True NEP_2 may be even lower.) The quantum efficiency due to coupling of bowtie antenna with QDs has not been systematically studied, and the antenna structure of the devices is far from optimum. If $\eta =$ 0.01 is assumed in (22), one has $\mathrm{NEP}_1 = 4.5 \times 10^{-21}$ W/Hz$^{1/2}$ (the DQD detector) and 4.3×10^{-21} W/Hz$^{1/2}$ (the SQD detector) [22]. It may not be difficult to achieve substantially lower values of NEP_1 by improving antenna design.

The sensitivity of CSIPs ($h\nu = 84$ meV, $\lambda = 14.7$ μm) has been studied experimentally by using a calibrated blackbody radiation emitter. In devices with $L \times W = 16 \times 4\,\mu\mathrm{m}^2$ and $1.5 \times 0.8\ \mu\mathrm{m}^2$, $\Gamma \approx$ 0.5/s and 0.033/s were found, respectively, at $T =$ 4.2 K, which yield $\mathrm{NEP}_2 = 1.4 \times 10^{-20}$ W/Hz$^{1/2}$ ($L \times W = 16$ $\times 4\,\mu\mathrm{m}^2$) and 3.6×10^{-21} W/Hz$^{1/2}$ ($L \times W = 1.5 \times 0.8\,\mu\mathrm{m}^2$). The quantum efficiency was determined to be $\eta = 2.0\%$ in the device ($L \times W = 16 \times 4\ \mu\mathrm{m}^2$) with a microstrip antenna coupler, leading to $\mathrm{NEP}_1 = 6.8 \times 10^{-19}$ W/Hz$^{1/2}$. No doubt a substantially lower value ($\mathrm{NEP}_1 = 1.9 \times 10^{-19}$ W/Hz$^{1/2}$) will be achieved if an improved metal mesh coupler ($\eta = 7.0\%$) is adopted.

Johnson noise $\langle I^2_{\mathrm{Johnson}}\rangle/\Delta f = 4k_BT/Z = (4ne\mu W/L)k_BT$ and shot noise $\langle I^2_{\mathrm{shot}}\rangle/\Delta f = 2eI = 2ne^2\mu WV_{SD}/L$, with Boltzmann constant k_B provide two dominant contributions to the noise current in CSIPs. By replacing $\langle I_n^2\rangle$ in (24) with the aforementioned expressions, theoretically expected NEPs are derived as

$$\mathrm{NEP}_{\mathrm{Johnson}} = \left\{\left(\frac{W}{L}\right)ne\mu\right\}^{1/2}\left(\frac{h\nu}{eG_{\mathrm{PC}}}\right)(4k_BT)^{1/2} \tag{25}$$

$$\mathrm{NEP}_{\mathrm{shot}} = \left\{\left(\frac{W}{L}\right)ne\mu\right\}^{1/2}\left(\frac{h\nu}{eG_{\mathrm{PC}}}\right)(2eV_{SD})^{1/2} \tag{26}$$

where

$$G_{\mathrm{PC}} = \frac{\left(\alpha^2\tau_{\mathrm{reset}}\mu V_{SD}\right)}{2L^2}$$

from (14)–(17) and (21). Equations (25) and (26) show that NEP $\propto (WL^3n/\mu)^{1/2}$. Assuming $\mu = 10$ m^2/Vs, $n = 2 \times 10^{15}$/m^2 and $\alpha = 1$ and considering a measurement of 100-ms time constant ($\tau_{\mathrm{reset}} = 200$ ms) with $V_{SD} = 20$ mV at $T =$ 4.2 K, one obtains $\mathrm{NEP}_{\mathrm{Johnson}} = 4.6 \times 10^{-22}$ W/Hz$^{1/2}$ and $\mathrm{NEP}_{\mathrm{shot}} = 2.5 \times 10^{-21}$ W/Hz$^{1/2}$ for a device of $L \times W =$ $16 \times 4\ \mu\mathrm{m}^2$, and even still lower values $\mathrm{NEP}_{\mathrm{Johnson}} = 6.0 \times 10^{-24}$ W/Hz$^{1/2}$ and $\mathrm{NEP}_{\mathrm{shot}} = 3.2 \times 10^{-23}$ W/Hz$^{1/2}$, for the smaller device of $L \times W = 1.5 \times 0.8\ \mu\mathrm{m}^2$. It should be noted that these surprisingly low values of theoretical NEPs are expected not for state-of-the-art 2DEG layer but for a standard one ($\mu = 10$ m^2/Vs and $n = 2 \times 10^{15}$/m^2). It is also not difficult to fabricate a device smaller than $L \times W = 1.5 \times 0.8\ \mu\mathrm{m}^2$, which will give even smaller NEP. These results clearly demonstrate the incomparable advantage of CSIPs as highly sensitive detectors, and strongly suggest that the performance of real devices will be significantly improved in the future.

Experimental NEP values in the table demonstrate incomparable sensitivity of these detectors, to which no other existing detectors may compete in corresponding wavelengths. In a state-of-the-art superconducting hot-electron nanobolometer, theoretical values of $\mathrm{NEP}_{\mathrm{theory}} \approx$ (9–200) $\times 10^{-21}$ W/Hz$^{1/2}$ due to thermal energy fluctuation are suggested [11]. In the QD detectors, however, even the experimentally achieved values are lower than those theoretically suggested NEP values. Though not written in the table, theoretically expected NEP values of the QD detectors would be less than 10^{-25} W/Hz$^{1/2}$. The large discrepancy between the experimental and theoretical values of NEP strongly suggest that crystal imperfections like electron traps significantly affect the noise current or the dark switching event in true devices. In other words, it is

probable that the sensitivity be significantly improved via material engineering.

It is to be mentioned for CSIPs that NEP $\propto 1/\tau_{\rm life} \propto 1/\tau_{\rm reset}$ in general, and that the detection speed has to be sacrificed to achieve highest sensitivity. Actually, however, this may not substantially restrict applicability of the CSIP because high-speed measurements are usually important in conditions where the radiation is not too faint.

VI. Summary

A series of semiconductor THz single-photon detectors have been described. The detection sensitivity demonstrated in these detectors is, in terms of NEP, more than orders of magnitude superior to any other detectors. Another remarkable strength is the huge signal amplitude, which is a consequence of a large-current responsivity or the large-photoconductive gain. This, together with the low output impedance of the detectors ($Z \approx$ 200 kΩ: QD detectors, $Z \approx$ 0.1–10 kΩ: CSIPs), makes these devices truly unique detectors. That is, the signals are so robust that they can be treated with extremely simple circuits. In fact, a single-photon-induced current pulse (step) can be recorded with a conventional voltage or current amplifier operating at room temperature, where the signal is guided from the detector to the amplifier by using an approximately 2-m-long twisted-pair lead: all the experimental data shown in this paper have been taken in such a scheme.

The theoretical limit of the sensitivity of both the QD detectors and CSIPs lies still far beyond the experimentally realized level. First, quantum efficiency for coupling with radiation may be improved largely by exploring optimum antenna/coupler structures. Second, higher quality crystals of GaAs/AlGaAs DQW heterostructures will lead to less noise current and lower rate of dark switching in CSIPs. In general, the sensitivity of CSIPs is expected to increase sharply with decreasing the detector size, namely, NEP $\propto W^{1/2}L^{3/2}$. For the design of small submicrometer CSIPs, a scheme in which excited electrons "laterally" escape from the isolated QW island [48] may be beneficial.

Expansion of the wavelength range is being attempted in CSIPs [46], [47]. The maximum operating temperature is expected to be roughly proportional to the photon energy. Noting $T \approx 25$ K for $\lambda = 15$ μm ($h\nu = 84$ meV) [42], the temperature is expected to range from $T \approx 50$ K for $\lambda = 8$ μm ($h\nu =$ 154 meV) to $T \approx 4$ K for $\lambda = 80$ μm ($h\nu = 15.4$ meV). Owing to the simple device structure, CSIPs are promising for integration to large-scale arrays. Monolithic integration with GaAs LSIs is also expected.

The THz single-photon detectors have opened up a new field of photon-counting THz imaging [12]–[14] as well as of sub-wavelength high-resolution passive THz microscopy [16]. On-chip manipulation of THz photons has also been demonstrated, providing a preliminary step for approaching an integrated on-chip THz-photon spectrometer [17]. An important potential application of the THz single-photon detectors is certainly astrophysics, especially for space observatory [50]. In addition to what have been described earlier, the THz photon-counting detectors will no doubt have further versatile applications in the future.

Acknowledgment

The author would like to thank valuable contributions of O. Astavief, V. Antonov, Z. An, J.-C. Chen, T. Ueda, P. Nickels, and Z. Wang for their valuable contributions. This paper is based on the collaborating work with a number of researchers.

References

[1] I. Prochazka, "Semiconducting single photon detectors: The state of the art," *Phys. Stat. Sol. (c)*, vol. 2, no. 5, pp. 1524–1532, 2005.

[2] A. Korneev, P. Kouminov, V. Matvienko, G. Chulkova, K. Smirnov, B. Voronov, G. N. Gol'tsman, M. Currie, W. Lo, K. Wilsher, J. Zhang, W. Słysz, A. Pearlman, A. Verevkin, and R. Sobolewskic, "Sensitivity and gigahertz counting performance of NbN superconducting single-photon detectors," *Appl. Phys. Lett.*, vol. 84, no. 26, pp. 5338–5340, 2004.

[3] A. Engel, A. Semenov, H. W. Hübers, K. Il'in, and M. Siegel, "Superconducting single-photon detector for the visible and infrared spectral range," *J. Mod. Opt.*, vol. 51, no. 9–10, pp. 1459–1466, 2004.

[4] T. Nakagawa and H. Murakami, "Mid- and far-infrared astronomy mission SPICA," *Adv. Space Res.*, vol. 40, pp. 679–683, 2007.

[5] R. J. Schoelkopf, S. H. Moseley, C. M. Stahle, P. Wahlgren, and P. Delsing, "A concept for a submillimeter-wave single-photon counter," *IEEE Trans. Appl. Supercond.*, vol. 9, no. 2, pp. 2935–2939, Jun. 1999.

[6] S. Komiyama, O. Astavief, V. Antonov, T. Kutsuwa, and T. Hirai, "A single-photon detector in the far-infrared range," *Nat. (Lond.)*, vol. 403, pp. 405–407, 2000.

[7] O. Astavief, S. Komiyama, T. Kutsuwa, V. Antonov, Y. Kawaguchi, and K. Hirakawa, "Single-photon detector in the microwave range," *Appl. Phys. Lett.*, vol. 80, pp. 4250–4252, 2002.

[8] H. Hashiba, V. Antonov, L. Kulik, A. Tzalenchuk, P. Kleindschmid, S. Giblin, and S. Komiyama, "Isolated quantum dot in application to terahertz photon counting," *Phys. Rev. B*, vol. 73, pp. 081310-1–081310-4, 2006.

[9] T. Ueda, Z. An, S. Komiyama, and K. Hirakawa, "Charge-sensitive infrared phototransistors: Characterization by an all-cryogenic spectrometer," *J. Appl. Phys.*, vol. 103, pp. 093109-1–093109-7, 2008.

[10] P. K. Day, H. G. LeDuc, B. A. Mazin, A. Vayonakis, and J. Zmuidzinas, "A broadband superconducting detector suitable for use in large arrays," *Nature*, vol. 425, pp. 817–821, 2003.

[11] J. Wei, D. Olaya, B. S. Karasik, S. V. Pereverzev, A. V. Sergeev, and M. E. Gershenson, "Ultrasensitive hot-electron nanobolometers for terahertz astrophysics," *Nat. Nanotechnol.*, vol. 3, pp. 496–500, 2008.

[12] K. Ikushima, Y. Yoshimura, T. Hasegawa, S. Komiyama, T. Ueda, and K. Hirakawa, "Photon-counting microscopy of terahertz radiation," *Appl. Phys. Lett.*, vol. 88, pp. 152110-1–152110-3, 2006.

[13] K. Ikushima, H. Sakuma, Y. Yoshimura, S. Komiyama, T. Ueda, and K. Hirakawa, "THz imaging of cyclotron emission in quantum Hall conductors," *Phys. E*, vol. 34, pp. 22–26, 2006.

[14] K. Ikushima, S. Komiyama, T. Ueda, and K. Hirakawa, "THz-photon generation due to electrons injected via quantum-Hall edge channels," *Phys. E*, vol. 40, pp. 1026–1029, 2008.

[15] Y. Kajihara, S. Komiyama, P. Nickels, and T. Ueda, "A passive long-wavelength infrared microscope with a highly sensitive Phototransistor," *Rev. Sci. Instrum.*, vol. 80, pp. 063702-1–063702-4, 2009.

[16] Y. Kajihara, S. Komiyama, P. Nickels, and T. Ueda, "A sensitive near-field microscope for thermal radiation," *Rev. Sci. Instrum.*, vol. 81, pp. 033706-1–033706-4, 2010.

[17] K. Ikushima, D. Asaoka, S. Komiyama, T. Ueda, and K. Hirakawa, "Manipulating terahertz photons on a quantum Hall effect device," *Physica E*, vol. 42, pp. 1034–1037, 2010, (presented at the 18th Int. Conf. Electronic Properties of Two-Dimensional Systems (EP2DS-18), Kobe, Japan, Jul. 20–24, 2009).

[18] Z. An, J. C. Chen, T. Ueda, S. Komiyama, and K. Hirakawa, "Infrared phototransistor using capacitively coupled two-dimensional electron gas layers," *Appl. Phys. Lett.*, vol. 86, pp. 172106-1–172106-3, 2005.

[19] A. Rose, *Concepts in Photoconductivity and Allied Problems*. New York: Interscience, 1963.

[20] L. L. Sohn, L. P. Kouwenhoven, and G. Schön, *Mesoscopic Electron Transport*, L. L. Sohn, L. P. Kouwenhoven, and G. Schön, Eds. Dordrecht, The Netherlands: Kluwer, 1997, pp. 105–214.
[21] K. K. Likharev, "Single-electron devices and their applications," *Proc. IEEE*, vol. 87, no. 4, pp. 606–632, Apr. 1999.
[22] O. Astafiev and S. Komiyama, "Single-photon detection with quantum dots in the far-infrared/submillimeter-wave range," in *Electron Transport in Quantum Dots*, J. P. Bird, Ed. Dordrecht, The Netherlands: Kluwer, 2003, ch. 9, pp. 363–396.
[23] Y. Kawano, T. Fuse, S. Toyokawa, T. Uchida, and K. Ishibashi, "Terahertz photon-assisted tunneling in carbon nanotube quantum dots," *J. Appl. Phys.*, vol. 103, pp. 034307-1–034307-5, 2008.
[24] J. M. Hergenrother, J. G. Lu, M. T. Tuominen, D. C. Ralph, and M. Tinkham, "Photon-activated switch behavior in the single-electron transistor with a superconducting island," *Phys. Rev. B*, vol. 51, pp. 9407–9410, 1995.
[25] O. Astafiev, V. Antonov, T. Kutsuwa, and S. Komiyama, "Far-infrared spectroscopy of single quantum dots in high magnetic fields," *Phys. Rev. B*, vol. 65, pp. 085315-1–085315-4, 2002.
[26] R. J. Schoelkopf, P. Wahlgren, A. A. Kozhevnikov, P. Delsing, and D. E. Prober, "The radio-frequency single-electron transistor (RF-SET): A fast and ultrasensitive electrometer," *Science*, vol. 280, pp. 1238–1242, 1998.
[27] T. Fujisawa and Y. Hirayama, "Charge noise analysis of an AlGaAs/GaAs quantum dot using transmission-type radio-frequency single-electron transistor technique," *Appl. Phys. Lett.*, vol. 77, pp. 543–545, 2000.
[28] O. Astafiev, V. Antonov, T. Kutsuwa, and S. Komiyama, "Electrostatics of quantum dots in high magnetic fields and single far-infrared photon detection," *Phys. Rev. B*, vol. 62, pp. 16731–16743, 2000.
[29] H. Hashiba, L. Kulik, V. Antonov, S. Komiyama, and C. Stanley, "Highly sensitive detector for submillimeter wavelength range," *Appl. Phys. Lett.*, vol. 85, pp. 6036–6038, 2004.
[30] P. Kleinschmidt, S. Giblin, A. Tzalenchuk, H. Hashiba, V. Antonov, and S. Komiyama, "Sensitive detector for a passive terahertz imager," *J. Appl. Phys.*, pp. 114504-1–114504-5, 2006.
[31] P. Kleinschmidt, S. Giblin, V. Antonov, H. Hashiba, L. Kulik, A. Tzalenchuk, and S. Komiyama, "A highly sensitive detector for radiation in the terahertz region," *IEEE Trans. Instr. Meas.*, vol. 56, no. 2, pp. 463–467, Apr. 2007.
[32] H. Hashiba1, V. Antonov1, L. Kulik, A. Tzalenchuk3, and S. Komiyama, "Sensing individual terahertz photons," *Nanotechnology*, vol. 21, pp. 165203-1–165203-5, 2010.
[33] W. Lu, A. J. Rimberg, K. D. Maranowski, and A. C. Gossard, "Single-electron transistor strongly coupled to an electrostatically defined quantum dot," *Appl. Phys. Lett.*, vol. 77, pp. 2746–2748, 2000.
[34] J. C. Chen, Z. An, T. Ueda, S. Komiyama, and V. Antonov, "Metastable excited states of a closed quantum dot probed by an aluminum single-electron transistor," *Phys. Rev. B*, vol. 74, pp. 045321-1–045321-5, 2006.
[35] T. A. Fulton and G. J. Dolan, "Observation of single-electron charging effects in small tunnel junctions," *Phys. Rev. Lett.*, vol. 59, pp. 109–112, 1987.
[36] P. W. Barone, S. Baik, D. A. Heller, and M. S. Strano, "Near-infrared optical sensors based on single-walled carbon nanotubes," *Nat. Mater.*, vol. 4, pp. 86–92, 2005.
[37] Y. Kawano, T. Uchida, and K. Ishibashi, "Terahertz sensing with a carbon nanotube/two-dimensional electron gas hybrid transistor," *Appl. Phys. Lett.*, vol. 95, pp. 083123-1–083123-3, 2009.
[38] S. Pelling, R. Davis, L. Kulik, A. Tzalenchuk, S. Kubatkin, T. Ueda, S. Komiyama, and V. N. Antonov, "Point contact readout for a quantum dot terahertz sensor," *Appl. Phys. Lett.*, vol. 93, pp. 073501-1–073501-3, 2008.
[39] Z. An, T. Ueda, J.-C. Chen, and S. Komiyama, "A sensitive double quantum well mid-infrared phototransistor," *J. Appl. Phys.*, vol. 100, pp. 044509-1–044509-7, 2006.
[40] Z. An, T. Ueda, S. Komiyama, and K. Hirakawa, "Metastable excited states of a closed quantum dot with high sensitivity to infrared photons," *Phys. Rev. B*, vol. 75, pp. 085417-1–085417-7, 2007.
[41] Z. An, T. Ueda, S. Komiyama, and K. Hirakawa, "Reset operation of quantum well infrared phototransistors," *IEEE Trans. Electron Devices*, vol. 54, no. 7, pp. 1776–1780, Jul. 2007.
[42] T. Ueda, S. Komiyama, Z. An, N. Nagai, and K. Hirakawa, "Temperature dependence of the performance of charge-sensitive infrared phototransistors," *J. Appl. Phys.*, vol. 105, pp. 064517-1–064517-8, 2009.
[43] P. Nickels, S. Matsuda, T. Ueda, Z. An, and S. Komiyama, "Metal hole arrays as a resonant photo-coupler for charge sensitive infrared phototransistors," *IEEE J. Quantum Electron.*, vol. 46, no. 3, pp. 384–390, Mar. 2010.
[44] S.-H. Yang and K.-R. Cho, "High dynamic range CMOS image sensor with conditional reset," in *Proc. IEEE 2002 Custom Integr. Circuit Conf.*, 2002, pp. 265–268.
[45] Z. An, private communication, 2010.
[46] Y. Soh, S. Komiyama, and T. Ueda, "A series of charge sensitive infrared phototransistors in a wide spectral range," *J. Infrared, Milimeter, Terahertz Waves*, 2010, to be published.
[47] Z. Wang *et al.*, "Charge Sensitive Infrared Phototransistor for 45 μm Wavelength," *J. Appl. Phys.*, vol. 107, pp. 1–4, 2010.
[48] Z. Wang, S. Komiyama, T. Ueda, and N. Nagai, "A modified scheme of charge sensitive infrared phototransistor," *Appl. Phys. Lett.*, vol. 95, pp. 022112-1–022112-3, 2009.
[49] P. L. Richards, "Bolometers for infrared and millimeter waves," *J. Appl. Phys.*, vol. 76, pp. 1–24, 1994.
[50] Y. Doi, Z. Wang, T. Ueda, P. Nickels, S. Komiyama, M. Patrashin, I. Hosako, S. Matsuura, M. Shirahata, Y. Sawayama, and M. Kawada, "CSIP: A novel photon-counting detector applicable for the SPICA far-infrared instrument," in *Proc. SPICA Joint Eur. Jpn. Workshop*, Oxford, U.K.: Oxford University Press, 2009, pp. 05003-1–05003-4.

Susumu Komiyama received the B.S., M.S., and Ph.D. degrees, in 1971, 1973, and 1976, respectively, all from the University of Tokyo, Tokyo, Japan.

From 1979 to 1981, he was with Hamburg University, Germany. During 1976–1982, at the early stage of his career, he was engaged in research on nonlinear transport phenomena and discovered streaming motion and population inversion of hot carriers in ionic crystals and in semiconductors. Since 1982, he has been a Faculty Member at the Department of Basic Science, University of Tokyo, where he has been engaged in research on quantum Hall effects of two-dimensional electron gas systems and semiconductor quantum dots. He is a pioneer of developing p-type germanium terahertz lasers (1982–1992) as well as single-terahertz photon detectors based on quantum dots (2000) and CSIPs (2005). He is currently engaged in research on establishing passive terahertz microscopy.